CFD Letters www.cfdl.issres.net Vol. 3 (1) – March 2011

Simulating Multiphase Flows in Porous Media with High Order CE/SE Method

Yang Duo-Xing[1c] and Zhang De-liang[2]

[1] *Institute of Crustal Dynamics, CEA, Beijing, 100085 CHINA*
[2] *LHD Institute of Mechanics, CAS, Beijing, 1000190 CHINA*

Received: 18/10/2010 – Revised 24/12/2010 – Accepted 17/02/2011

Abstract

In this paper, an updated CE/SE (space-time conservation element and solution element) scheme with second order accuracy is constructed on hexahedral grids and is extended to solve multiphase flows in porous media. The hybrid particle level set method is modified and applied for tracing the interfaces of fluids. Three benchmark problems are simulated numerically and the computational results are carefully compared with the results from other literature. Based on the single phase lid-driven cavity problem, the model of dual layer lid-driven cavity flow in porous media is also proposed as a benchmark problem. Results demonstrate that the computational scheme developed currently is high accurate, reliable and efficient for the porous multiphase flow problems considered.

Keywords: Multiphase flow; CE/SE method; porous media

1. Introduction

The multiphase flows in porous media are highly nonlinear phenomena and hardly described by analytical solutions. Hence numerical methods have to be proposed and applied. However, two primary challenges are still confronted in the numerical methods, including the numerical scheme for the governing equations and the special treatments for the fluid-fluid interfaces. The governing equations for the multiphase flows in porous media can be traditionally formulated in two ways known as Lagrangian and Eulerian method.

For the Lagrangian approach, the meshes are fixed within and deformed with the fluid. The well-known Lagrangian scheme is the Lattice Boltzmann method. Up to now, several lattice Boltzmann models (LBM) have been proposed for fluids flow in porous media. Typically, a generalized lattice Boltzmann model (GLBM) was proposed for isothermal incompressible flow through porous media by Guo and Zhao [1]. Yan et al. [2] used GLBM for simulation of air flows in heterogeneous porous media. The main limitation of the Lagrangian approach is that the results are inaccurate with using the finite difference approximation when the grid cells are distorted significantly [3].

In the Eulerian approach, the grids are fixed in space through which fluids flow. Deiber and Bortolozzi [4] applied vorticity-stream function scheme to study natural convection in a porous

[c] Corresponding Author: Yang Duo-Xing
Email: yangdx@mail.iggcas.ac.cn
 PII: S2180-1363(11)3101-X

annulus. Sman [5] numerically solved the DFB model with 3D finite element solver (FIDAP). Costa et al. [6] used the control volume based finite element method to simulate non-Darcian flows through spaces partially filled with a porous media. Reis et al. [7] applied the finite volume method to simulate the impact of liquid droplets on porous surfaces. Karim et al. [8] applied the simplified marker and cell (SMAC) method to simulate wave transformation in porous structure using volume of fluid (VOF) based two-phase fluid model. But it is difficult to identify the material interfaces accurately at each time step. Therefore, a high-accuracy fluid-fluid interface tracing algorithm must be adopted for the Eulerian approach.

The CE/SE method (the space—time Conservation Element and Solution Element method) originally proposed by Chang [9,10] is a novel high-resolution CFD method for hyperbolic conservation laws. It substantially differs from other traditional well-established methods. It has many features, such as a unified treatment of space and time, satisfying both local and global flux conservation in space and time by introduction of the Solution Elements (SEs) and Conservation Elements (CEs). The CE/SE method has been extended to a high-order scheme [11]. Chang et al. [12] used this method for the aeroacoustic computations; Guo et al. [13] extended the CE/SE method to viscous flows. Recently, Wang et al. [3] proposed an updated first order accuracy CE/SE scheme and employed to solve the complex elastic–plastic flows with solid features; Yang et al. [14] extended the updated CE/SE approach to solve single phase flows in porous media, and Yang et al. [15] introduced the updated CE/SE scheme into simulation of multiphase flows in porous media. Zhang et al. [16] developed a second order accuracy CE/SE based on hexahedral grids. However, to our best knowledge, the CE/SE method with second order accuracy has not been employed to solve the complex multiphase flows in porous media.

The Level Set method (LS) [17] is effective for tracing moving interfaces of fluids. The main idea of the Level Set method lies in introduction of the implicit function to describe the advection of a certain interface. The LS is appropriate to capture the interfaces undergoing extremely topological changes. The hybrid particle Level Set method (HPLS) was developed by Enright et al. [18], combining the advantages of the Eulerian Level Set approach and the Lagrangian method based on marker particles, which is a robust technique to overcome the issue of mass loss (volume loss for the incompressible case).

In the present work, we propose a new definition of SE and CE and construct an improved CE/SE scheme with second order accuracy. The new definition is based on the hexahedron mesh. Furthermore, we apply the improved CE/SE scheme to solve the problems of two-dimensional multiphase flows in porous media. The hybrid particle Level Set approach is employed for tracing fluid-fluid interfaces. For verifying the accuracy, resolution, and efficiency of the improved CE/SE scheme, we simulate the well-known Taylor instability problem and the transformation and motion of droplets by gravity. The computational results are carefully compared with the results from other literature. We finally simulate the shear-driven flow in a dual layer square cavity in which deformation of interface and streamlines are fully manifested.

2. Numerical methods

2.1 Governing equations

We assume that (1) the supercritical CO2 and brine water are immiscible, and the saline aquifer is the isotropic and homogeneous porous media. Thermal equalibrium is also assumed. (2) the two fluids are viscous, Newtonian and incompressible, (3) the flow is isothermal, the interface tension is taken as constant and there is no interfacial resistance to mass transfer, and (4) mass transfer is assumed to have no effect on the physical properties of the system. By employing a CSF (continuum surface force) model [19] of the surface tension force for the level set approach [17], the surface tension is reformulated as a volume force.

$$\vec{F}_{SV} = k(\phi)\delta_{\alpha}(\phi)\nabla\phi \tag{1}$$

Where ϕ is a smooth level set function, which is positive outside the interface, negative inside the interface and zero at the interface, δ is a surface tension delta function and κ is the interface front curvature. In a two-dimensional coordinate system, mass and momentum conservation [15] with the level set approach incorporated are written in terms of dimensionless variables as

$$\frac{\partial u_i}{\partial x_i} = 0 \tag{2}$$

$$\frac{\partial u_i}{\partial t} + \frac{\partial}{\partial x_j}(\frac{1}{\varphi}u_i u_j) = -\frac{1}{\bar{\rho}}\frac{\partial P}{\partial x_i} + \frac{1}{\varphi\bar{\rho}R_e}\frac{\partial}{\partial x_j}(\bar{\mu}(\frac{\partial u_i}{\partial x_j} + \frac{\partial u_j}{\partial x_i})) - \varphi\frac{g_i}{F_r} - \varphi\frac{k(\phi)\delta(\phi)\nabla\phi}{\bar{\rho}W_e} - \frac{1}{D_a R_e}u_i - \frac{\varphi F_b}{\sqrt{D_a}}u_i\sqrt{u_i^2 + u_j^2} \tag{3}$$

with dimensionless groups of the Reynolds, Froude, Weber numbers, Darcy number and inertial factor as $\mathrm{Re} = \frac{\rho_o LU}{\mu_o}$, $Fr = \frac{U^2}{gL}$, $We = \frac{\rho_o LU^2}{\sigma_o}$, $Da = \frac{K}{L^2}$ and $F_b = \frac{1.75}{\sqrt{150\phi^3}}$ respectively. $\bar{\rho}, \bar{\mu}$ are the dimensionless ratios of the viscosity and density.φ is the porosity and K is the permeability. For simplicity, hereafter we denote λ_ρ and λ_μ as $\bar{\rho}$ and $\bar{\mu}$ respectively. To prevent numerical instability, it is necessary to smooth the values of the density ρ_ε and viscosity μ_ε as:

$$\rho_\varepsilon(\phi) = \lambda_\rho + (1-\lambda_\rho)H_\varepsilon(\phi)$$
$$\mu_\varepsilon(\phi) = \lambda_\mu + (1-\lambda_\mu)H_\varepsilon(\phi) \tag{4}$$

Where the Heaviside function [18] $H_\varepsilon(\phi)$ is formulated as followings:

$$H_e(\phi) = \begin{cases} 0 & \phi < -\varepsilon \\ \frac{1}{2}(1 + \frac{\phi}{\varepsilon} + \frac{1}{\pi}\sin(\frac{\pi\phi}{\varepsilon})) & |\phi| \le \varepsilon \\ 1 & \phi > \varepsilon \end{cases} \tag{5}$$

The following equation will evolve the zero level set function [15]:

$$\varphi\frac{\partial\phi}{\partial t} + u_i\frac{\partial\phi}{\partial x_i} = 0 \tag{6a}$$

The above level set equation is solved using a five-order WENO discretization and Runge-Kutta method [20]. Yang et al. [21] presented a reinitialization equation insure that values for level set function will not be greatly distorted. The numerical discretization of the reinitialization equation of the level set function will not preserve the total mass conservation. To overcome this difficulty, the Particle level set method [18] can be presented to conduct the solution of the reinitialization equation. The hybrid particle Level Set method is a coupling method of Lagrangian method and Eulerian method, which merges the best aspects of Eulerian front capturing schemes and Lagrangian front-tracking methods for improved mass conservation in a fluid flow. Massless marker particles were inserted to correct mass loss in level set function by using the characteristic information of the escaped massless marker (as shown in figure1). The particle level set method maintains the nice geometric properties of level set method, and performs favourably in the conservation of mass and for interface resolution. The particle Lagrangian function [18] is written as:

$$\frac{d\bar{r}_p}{dt} = \vec{V}(\bar{r}_p) \tag{6b}$$

where is $\bar{r}_p$ the location of the particle, and $\bar{V}$ is the particle velocity. The third-order Runge-Kutta scheme is used to solve Equation6b.

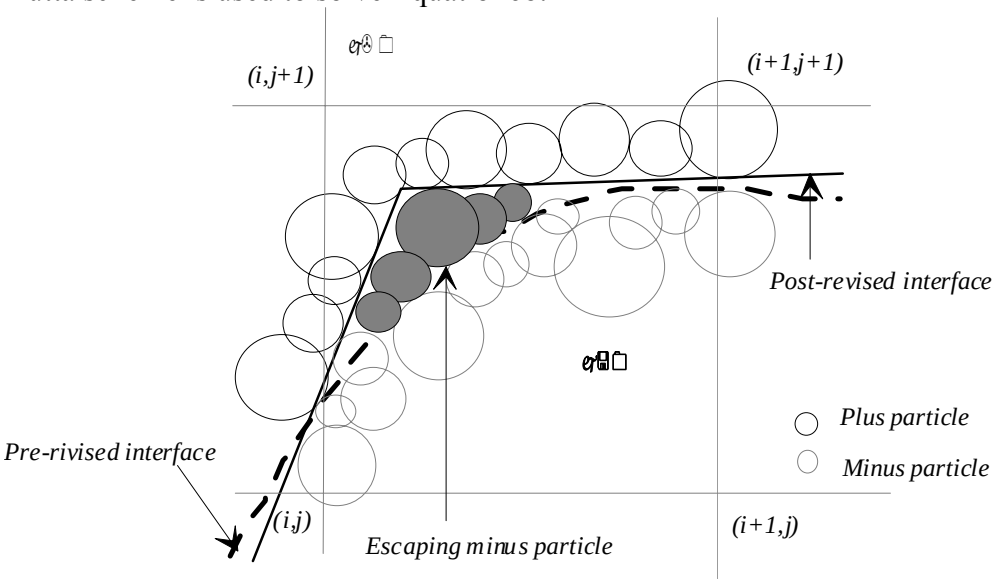

Figure1. Schematic map of the hybrid particle Level-Set method (HPLS)

2.2 Improved CE/SE scheme with the second order accuracy

An updated CE/SE scheme based on hexahedral grids is proposed. The SE (Solution Elements) and CE (Conservation Elements) are demonstrated in figure2.
The governing equation(1) and equation(2) can be rewritten as the Euler equation [14]

$$\frac{\partial \mathbf{Q}}{\partial t}+\frac{\partial \mathbf{E}(\mathbf{Q})}{\partial x}+\frac{\partial \mathbf{F}(\mathbf{Q})}{\partial y}=\mathbf{S}(\mathbf{Q}) \tag{7}$$

where $\mathbf{Q}, \mathbf{E}, \mathbf{F}, \mathbf{S}$ are vectors of primary variable, flux in x-direction, flux in y-direction and source, respectively. Let (j,k,n) denote a set of space-time mesh points, where $n=0,\pm\frac{1}{2},\pm 1,\pm\frac{3}{2}\ldots$ for time, $j=0,\pm\frac{1}{2},\pm 1,\pm\frac{3}{2}\ldots$ for x, $k=0,\pm\frac{1}{2},\pm 1,\pm\frac{3}{2}\ldots$ for y. A SE is defined as the vicinity of a mesh point and the whole space-time region is divided into non-overlapping CEs. Assume that the physical variables in every SE are approximated by the Taylor's expansions at the mesh point associated with the SE, and the conservation equation (4) is satisfied in every CE. Let $x_1=x, x_2=y, x_3=t$ be considered as the coordinates of a Euclidean space E_3. By means of the Gauss' divergence theorem, equation (7) is rewritten in form of

$$\oint_{S(V)} \mathbf{H}_m \cdot d\mathbf{s}=\int_V S_m dV \tag{8}$$

Where, $\mathbf{H}_m=(E_m,F_m,Q_m)$ is the space-time flux vector, here Q_m, E_m and F_m are the components of vector $\mathbf{Q}$, $\mathbf{E}$ and $\mathbf{F}$, and respectively., and S_m are the components of the source term vector. $S(V)$ is the boundary of an arbitrary space-time region V in E_3, $d\mathbf{s}=d\sigma\cdot\mathbf{n}$ with $d\sigma$ and $\mathbf{n}$, respectively, being the area and the outward unit normal of a surface element on $S(V)$. figure2(a) shows the projection of mesh points on the $x-y$ plane, in which the interval between the mesh points • and ○ is $\Delta t/2$ in the time direction or $\frac{1}{2}$ in the mesh number n. For any point $P'(j,k,n)$ on which the variables are solved, define the

solution element SE(P′) constituted by the three vertical planes intersecting at $P'\ (j,k,n)$ and their neighborhood space as demonstrated in figure2(b). Suppose that Q_m, E_m and F_m at point (t,x,y) in SE(P′) are approximated by the second-order Taylor expansions at $P'\ (j,k,n)$, i.e.,

$$\begin{aligned}
Q_m(dx,dy,dt)_{P'} &= (Q_m)_{P'} + (Q_{mx})_{P'}dx + (Q_{my})_{P'}dy + (Q_{mt})_{P'}dt \\
&+ \frac{1}{2}(Q_{mxx})_{P'}(dx)^2 + \frac{1}{2}(Q_{myy})_{P'}(dy)^2 + \frac{1}{2}(Q_{mtt})_{P'}(dt)^2 \\
&+ (Q_{mxt})_{P'}(dx\cdot dt) + (Q_{myt})_{P'}(dy\cdot dt) + (Q_{mxy})_{P'}(dx\cdot dy) \\
E_m(dx,dy,dt)_{P'} &= (E_m)_{P'} + (E_{mx})_{P'}dx + (E_{my})_{P'}dy + (E_{mt})_{P'}dt \\
&+ \frac{1}{2}(E_{mxx})_{P'}(dx)^2 + \frac{1}{2}(E_{myy})_{P'}(dy)^2 + \frac{1}{2}(E_{mtt})_{P'}(dt)^2 \\
&+ (E_{mxt})_{P'}(dx\cdot dt) + (E_{myt})_{P'}(dy\cdot dt) + (E_{mxy})_{P'}(dx\cdot dy) \qquad (9) \\
F_m(dx,dy,dt)_{P'} &= (F_m)_{P'} + (F_{mx})_{P'}dx + (F_{my})_{P'}dy + (F_{mt})_{P'}dt \\
&+ \frac{1}{2}(F_{mxx})_{P'}(dx)^2 + \frac{1}{2}(F_{myy})_{P'}(dy)^2 + \frac{1}{2}(F_{mtt})_{P'}(dt)^2 \\
&+ (F_{mxt})_{P'}(dx\cdot dt) + (F_{myt})_{P'}(dy\cdot dt) + (F_{mxy})_{P'}(dx\cdot dy)
\end{aligned}$$

Here, $dx = x - x_{P'}$, $dy = y - y_{P'}$, $dt = t - t_{P'}$, where $x_{p'}$, $y_{p'}$ and $t_{p'}$ are the position coordinates of point P'. Substituting equation (9) into equation (7) gives

$$\begin{aligned}
(Q_{mt})_{P'} &= -(E_{mx})_{P'} - (F_{my})_{P'} + (S_m)_{P'} \\
(Q_{mxt})_{P'} &= -(E_{mxx})_{P'} - (F_{mxy})_{P'} + (S_{mx})_{P'} \\
(Q_{myt})_{P'} &= -(E_{mxy})_{P'} - (F_{myy})_{P'} + (S_{my})_{P'} \\
(Q_{mtt})_{P'} &= -(E_{mxt})_{P'} - (F_{myt})_{P'} + (S_{mt})_{P'} \qquad (10)
\end{aligned}$$

The above equations imply that the variables required in computation are $(Q_m)_{P'}$, $(Q_{mx})_{P'}$ and $(Q_{my})_{P'}$, because S_m, E_m and F_m are the function of Q_m. Define the Conservation Element CE(P') as illustrated as figure2 (c). It can be seen from figure1(c) that CE(P') is related to not only SE(P′) but also the SEs of SE(A), SE(C), SE(E) and SE(G). Note that the values of physical variables on mesh point A,C,E and G are known. Assume that the integral conservation laws are satisfied in every CE. Integrating equation (8) on the surfaces of CE(P') with the aid of equation (9) , we find

$$\begin{aligned}
&(Q_m)_{P'} + \frac{1}{24}\frac{\Delta x}{\Delta y}(Q_{mxx})_{P'} + \frac{1}{24}\frac{\Delta y}{\Delta x}(Q_{myy})_{P'} - \frac{\Delta t}{4}(S_m)_{P'} \\
&\qquad = \frac{1}{4}(\overline{Q} + \frac{\Delta t}{\Delta x}\overline{E} + \frac{\Delta t}{\Delta y}\overline{F} + \frac{\Delta t}{4}\overline{S}) \qquad (11)
\end{aligned}$$

Where

$$\begin{aligned}
\overline{Q} &= Q_m(A,\frac{\Delta x}{4},\frac{\Delta y}{4},0) + Q_m(C,-\frac{\Delta x}{4},\frac{\Delta y}{4},0) + Q_m(E,-\frac{\Delta x}{4},-\frac{\Delta y}{4},0) + Q_m(G,\frac{\Delta x}{4},-\frac{\Delta y}{4},0) \\
\overline{E} &= E_m(A,0,\frac{\Delta y}{4},\frac{\Delta t}{4}) - E_m(C,0,\frac{\Delta y}{4},\frac{\Delta t}{4}) - E_m(E,0,-\frac{\Delta y}{4},\frac{\Delta t}{4}) + E_m(G,0,-\frac{\Delta y}{4},\frac{\Delta t}{4})) \\
\overline{F} &= F_m(A,\frac{\Delta x}{4},0,\frac{\Delta t}{4}) + F_m(C,-\frac{\Delta x}{4},0,\frac{\Delta t}{4}) - \qquad (12)
\end{aligned}$$

$$F_m(E,-\frac{\Delta x}{4},0,\frac{\Delta t}{4})-F_m(G,\frac{\Delta x}{4},0,\frac{\Delta t}{4})$$

$$\bar{S}=S_m(A)+S_m(C)+S_m(E)+S_m(G)$$

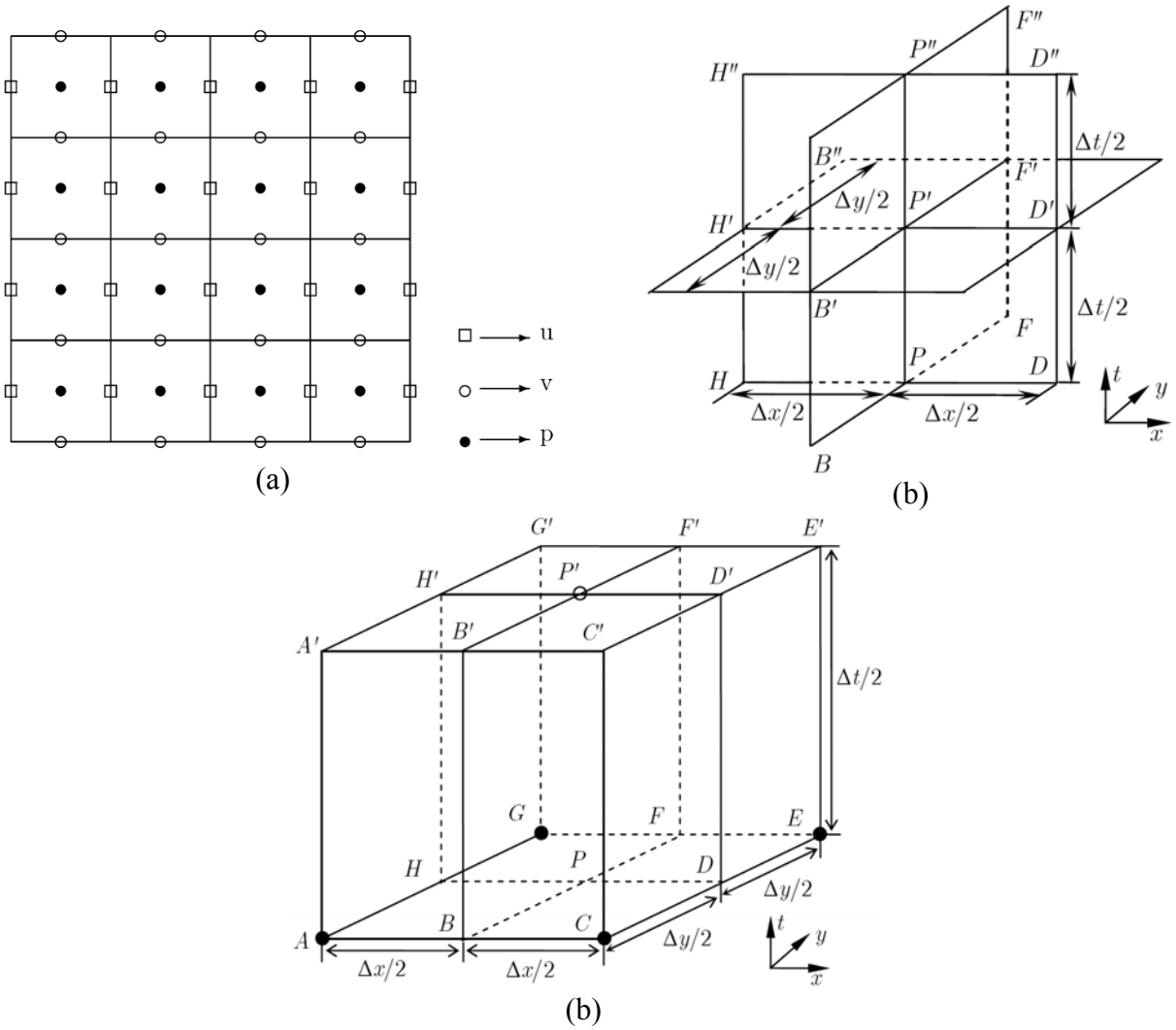

Figure 2. Mesh construction of the updated CE/SE method (a) mesh points, (b) SE (Solution Elements) and (c) CE (Conservation Elements)

Using the continuity conditions at points A', C', E' and G', the derivatives of Q_m with respect to x and y are obtained.

$$(Q_x)_{P'}=W[(Q_x)^-_{P'},(Q_x)^+_{P'},\alpha]$$

$$(Q_y)_{P'}=W[(Q_y)^-_{P'},(Q_y)^+_{P'},\alpha]$$

$$(Q_{mxx})_{P'}=\frac{1}{\Delta x}[(Q_{mx})_{D'}-(Q_{mx})_{H'}]$$

$$(Q_{myy})_{P'}=\frac{1}{\Delta y}[(Q_{my})_{F'}-(Q_{my})_{B'}]$$

$$(Q_{mxy})_{P'}=\frac{1}{2}[(\hat{Q}_{mxy})_{P'}+(\hat{Q}_{myx})_{P'}] \tag{13a}$$

Where

$$
\begin{aligned}
(Q_{mx})_{D'} &= [Q_{mx}(C,0,0,\Delta t/2) + Q_{mx}(E,0,0,\Delta t/2)]/2 \\
(Q_{mx})_{H'} &= [Q_{mx}(G,0,0,\Delta t/2) + Q_{mx}(A,0,0,\Delta t/2)]/2 \\
(Q_{my})_{F'} &= [Q_{my}(E,0,0,\Delta t/2) + Q_{my}(G,0,0,\Delta t/2)]/2 \\
(Q_{my})_{B'} &= [Q_{my}(A,0,0,\Delta t/2) + Q_{my}(C,0,0,\Delta t/2)]/2 \\
(\widehat{Q}_{mxy})_{P'} &= [Q_{mx}(C,0,0,\Delta t/2) - Q_{mx}(A,0,0,\Delta t/2) \\
&\quad + Q_{mx}(E,0,0,\Delta t/2) - Q_{mx}(G,0,0,\Delta t/2)]/(2\Delta y) \\
(\widehat{Q}_{myx})_{P'} &= [Q_{my}(C,0,0,\Delta t/2) - Q_{my}(A,0,0,\Delta t/2) \\
&\quad + Q_{my}(E,0,0,\Delta t/2) - Q_{my}(G,0,0,\Delta t/2)]/(2\Delta x)
\end{aligned}
\tag{13b}
$$

here $(Q_x)^{\pm}_{P'}$, $(Q_y)^{\pm}_{P'}$ are defined as such

$$
\begin{aligned}
(Q_{mx})^{-}_{P'} &= -\frac{1}{\Delta x}\left[Q_m(A,0,0,\frac{\Delta t}{2}) + Q_m(G,0,0,\frac{\Delta t}{2}) - 2(Q_m)_{P'} \right] \\
(Q_{mx})^{+}_{P'} &= +\frac{1}{\Delta x}\left[Q_m(C,0,0,\frac{\Delta t}{2}) + Q_m(E,0,0,\frac{\Delta t}{2}) - 2(Q_m)_{P'} \right] \\
(Q_{my})^{-}_{P'} &= -\frac{1}{\Delta y}\left[Q_m(A,0,0,\frac{\Delta t}{2}) + Q_m(C,0,0,\frac{\Delta t}{2}) - 2(Q_m)_{P'} \right] \\
(Q_{my})^{+}_{P'} &= +\frac{1}{\Delta y}\left[Q_m(E,0,0,\frac{\Delta t}{2}) + Q_m(G,0,0,\frac{\Delta t}{2}) - 2(Q_m)_{P'} \right]
\end{aligned}
\tag{13c}
$$

The weighted equation is $W[x_+, x_-, \alpha] = \dfrac{|x_+|^{\alpha} x_- + |x_-|^{\alpha} x_+}{|x_-|^{\alpha} + |x_-|^{\alpha}}$, and α is a constant (α = 2 in this study) [9].

It should be noted that $(Q_m)_{P'}$ can not be obtained explicitly form equation(11) due to the source term $(S_m)_{P'}$. As $(S_m)_{P'}$ is a function of $(Q_m)_{P'}$, a local Newton iterative procedure is usually needed to determine $(Q_m)_{P'}$. In the present work, to avoid the iterative procedure and save computation time, $(S_m)_{P'}$ is replaced by their linear prediction of current time in equation(11) [3,14,15],

$$
\begin{aligned}
&(Q_m)_{P'} + \frac{1}{24}\frac{\Delta x}{\Delta y}(Q_{mxx})_{P'} + \frac{1}{24}\frac{\Delta y}{\Delta x}(Q_{myy})_{P'} = \frac{1}{4}(\overline{Q} + \frac{\Delta t}{\Delta x}\overline{E} + \frac{\Delta t}{\Delta y}\overline{F}) + \frac{\Delta t}{8}\overline{S}) \\
&\widetilde{S} = \overline{S} + \frac{\Delta t}{4}\overline{S}_t
\end{aligned}
\tag{14}
$$

Where $\overline{S}_t$ is the time derivative of $\overline{S}$. $(Q_m)_{P'}$ can be directly solved without any iteration, since the time derivative of $(S_m)_A$, $(S_m)_E$, $(S_m)_C$ and $(S_m)_G$ are all known at current time.

2.3 Pretreatment method

The coupling between velocity and pressure is performed by artificial compressibility method [22] and the pretreatment method [14]. equation (15) can be rewritten in form of

$$
\phi\frac{\partial P}{\partial \tau} + C^2\rho(\frac{\partial u}{\partial x} + \frac{\partial v}{\partial y}) = 0 \tag{15}
$$

where τ is the visual time, and C^2 is the coefficient effecting the numerical stability. Substituting the visual time derivative of velocities into equation (15), we obtain

$$\frac{\partial \mathbf{U}}{\partial \tau}+\frac{\partial \mathbf{Q}}{\partial t}+\frac{\partial \mathbf{E}(\mathbf{Q})}{\partial x}+\frac{\partial \mathbf{F}(\mathbf{Q})}{\partial y}=\mathbf{S}(\mathbf{Q}) \tag{16}$$

here $\mathbf{U}=\begin{bmatrix}\frac{\phi}{C^2}P\\ u\\ v\end{bmatrix}$, for $\tau\to\infty$, equation (16) is consistent to equation (2). Applying the pressure splitting method , equation (16) takes the form

$$\frac{\partial \mathbf{U}_v}{\partial \tau}+\frac{\partial \mathbf{Q}_v}{\partial t}+\mathbf{R}_v(\mathbf{Q}_v)+\frac{\phi}{\rho}\nabla P=0 \tag{17}$$

where

$$\mathbf{R}_v(\mathbf{Q}_v)=(\frac{\partial \mathbf{E}_v(\mathbf{Q}_v)}{\partial x}+\frac{\partial \mathbf{F}_v(\mathbf{Q}_v)}{\partial y}-\mathbf{S}_v(\mathbf{Q}_v)),$$

$$\mathbf{Q}_v=\mathbf{U}_v=\begin{bmatrix}u\\ v\end{bmatrix},\quad \mathbf{E}_v=\begin{bmatrix}\frac{1}{\phi}u^2-\frac{\tau_{xx}}{\rho\,\mathrm{Re}}\\ \frac{1}{\phi}uv-\frac{\tau_{yx}}{\rho\,\mathrm{Re}}\end{bmatrix},\quad \mathbf{F}_v=\begin{bmatrix}\frac{1}{\phi}uv-\frac{\tau_{xy}}{\rho\,\mathrm{Re}}\\ \frac{1}{\phi}v^2-\frac{\tau_{yy}}{\rho\,\mathrm{Re}}\end{bmatrix}\text{ and}$$

$$\mathbf{S}_v=\begin{bmatrix}-\frac{\phi}{\rho Da\,\mathrm{Re}}u-\frac{\phi F_b}{\sqrt{Da}}u\sqrt{u^2+v^2}+\phi\frac{g_x}{Fr}\\ -\frac{\phi}{\rho Da\,\mathrm{Re}}v-\frac{\phi F_b}{\sqrt{Da}}v\sqrt{u^2+v^2}+\phi\frac{g_y}{Fr}\end{bmatrix}.$$

Using the time operator splitting method [15] to split pressure item in momentum equation (17), we obtain

$$\frac{\mathbf{Q}_v^{n+\frac{1}{2}}-\mathbf{f}(\mathbf{Q}_v^n)}{\Delta t}+\mathbf{R}_v^n(\mathbf{Q}_v^n)=0 \tag{18a}$$

$$\frac{\partial \mathbf{U}}{\partial \tau}+\frac{\mathbf{Q}_v^{n+1}-\mathbf{Q}_v^{n+\frac{1}{2}}}{\Delta t}+\frac{\phi}{\rho}\nabla P=0 \tag{18b}$$

We interpret equation (18a) as yielding an intermediate value of $\mathbf{Q}_v^n$, denoted by $\mathbf{Q}_v^{n+\frac{1}{2}}$ at time n. Here, the superscript n indicates the time step. $\mathbf{f}(\mathbf{Q}_v^n)$ is the value of $\mathbf{Q}_v^n$ at time step n. equation (18a) can be simulated by CE/SE method to obtain $\mathbf{Q}_v^{n+\frac{1}{2}}$. By means of time-marching solutions and internal iteration method, equation (12) and equation (18b) yield

$$\phi\frac{P^{m+1}-f(P^m)}{\Delta\tau}+C^2(\frac{\partial u}{\partial x}+\frac{\partial v}{\partial y})^m=0 \tag{19a}$$

$$\frac{\mathbf{U}^{m+1}-\mathbf{U}^m}{\Delta\tau}+\frac{\mathbf{Q}^{m+1}-\mathbf{Q}^{n+\frac{1}{2}}}{\Delta t}+\frac{\phi}{\rho}\nabla P^{m+1}=0 \tag{19b}$$

where m is the iteration step. Assume that we have already carried out m iteration.

Then, for the $m+1$ iteration, by substituting $\mathbf{Q}_v^{n+\frac{1}{2}}$ into equation (19a) and using CE/SE method, P^{m+1} can be calculated at iteration step $m+1$. Substituting P^{m+1} into equation (19b), $\mathbf{U}^{m+1}$ is obtained. The above procedure is repeated for a number of iteration, convergence is achieved when $\mathbf{U}^{m+1}-\mathbf{U}^m$ become less than a prescribed value (10^{-6}) at all grid points. After

convergence, $\mathbf{U}^{n+1}$ can be obtained at time step $n+1$. These governing equations are discretized on staggered orthogonal grid (as shown in figure 1(a) which eliminates the possibility of a checkerboard pressure pattern[3].

4. Numerical Validation

4.1 Taylor instability problem

Simulations of immiscible two-phase fluid flow instability were carried out to test the validity of the proposed CE/SE method. As the benchmark problem, Taylor instability problem [23] is commonly used to study the effects of fluid density differences (under the influence of gravity) and viscosity ratios on the stability/instability of immiscible flows. To initiate the instability at the fluid–fluid interface, the initially flat front was perturbed by a sinusoidal deformation [23]. Here, we considered displacement of a less dense fluid by a denser fluid. The ratio of viscosity and density are 1 and 3, respectively, for Re=1000. We assume that the porosity and Darcy number are 0.9 and 1.0×10^4, respectively [15]. The slip boundary conditions are applied to the left and right sides, while non-slip boundaries for the top and down sides. figure3 demonstrates that as time was increased, the mass interface varied from a single smooth finger to a highly unstable fragmented dendritic. The results are in excellent agreement with that obtained by Guermond [23].

4.2. Transformation and motion of droplets by gravity in porous media

The results of transformation and motion of droplets by gravity in porous media are shown in figure4. From figure4 we can find that the second-order accuracy CE/SE method and HPLS scheme performs well agreement with the results by FVM (Finite Volume Method) and Level Set method [24]. But the interfaces calculated by CE/SE are more accurate than that of FVM. It demonstrated that there is no discontinuity occurrence in the final deformed droplet calculated by CE/SE scheme. For both one and three droplets falling cases, the Darcy number and porosity are 10^4 and 0.9, respectively. Some implementation issues for droplets deformation are discussed in [15, 24]. We will not repeat the discussions.

4.3. Waves transportation in porous medium

The model was developed by coupling an ordinary porous flow model based on equations (2, 3,6,7) for porous media, and a two-phase flow model based on classical Navier–Stokes equations. A unique solution domain was established with proper treatment of the interface boundary between water, air and the structure [8]. The hybrid particle Level Set method was used to trace the interface between water and air. The resistance to flow caused by the presence of structural material was modeled in terms of drag and inertia forces. The updated CE/SE method and the hybrid particle Level-set method are used to calculate the wave height in both free and porous flows. The boundary and initial conditions as well as model parameters are found in the paper by Karim [8].For detailed information of model configuration of wave propagation in porous media, reader should refer to Karim et al. [8].

Here we complete the comparison of CE/SE calculated and measured non-dimensional wave heights for T = 1.6 s, H_I = 0.076 m, B/L = 0.5 [8], and porosity of 0.43. figure5 shows the CE/SE calculated wave height and the experimental results. It found that the wave height calculated by CE/SE in the clear flow domain is found identical to the experimental results. In the porous flow, the CE/SE calculated results are a little systematically higher than that of the experiment. The main reason results from the drag force components and inclusion of the

surface tension in the momentum equation. We can see the inertial coefficient is determined by F_b in our model, while Karim et al. [8] used numerical calibration technique to estimate the drag coefficients, which is not porosity dependent. Another key issue is that the surface tension mechanism is introduced in our model. Straughan [25] pointed that the surface tension in porous flows plays a vital role to determine the flow characteristics. From this point, it is reasonable to involve the surface tension in the momentum equations. Hence, it inferred that the method for the determination of drag coefficients are the primary contribution to the uncertainty of the CE/SE calculated wave heights in the porous media. Generally speaking, the updated CE/SE performed well.

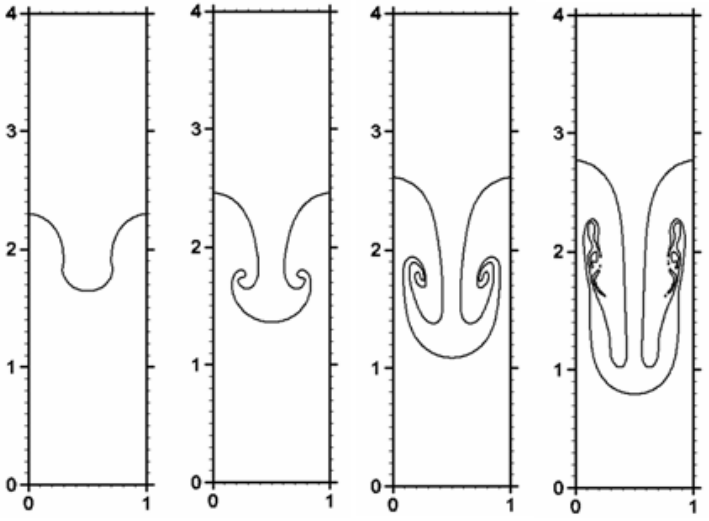

(a)

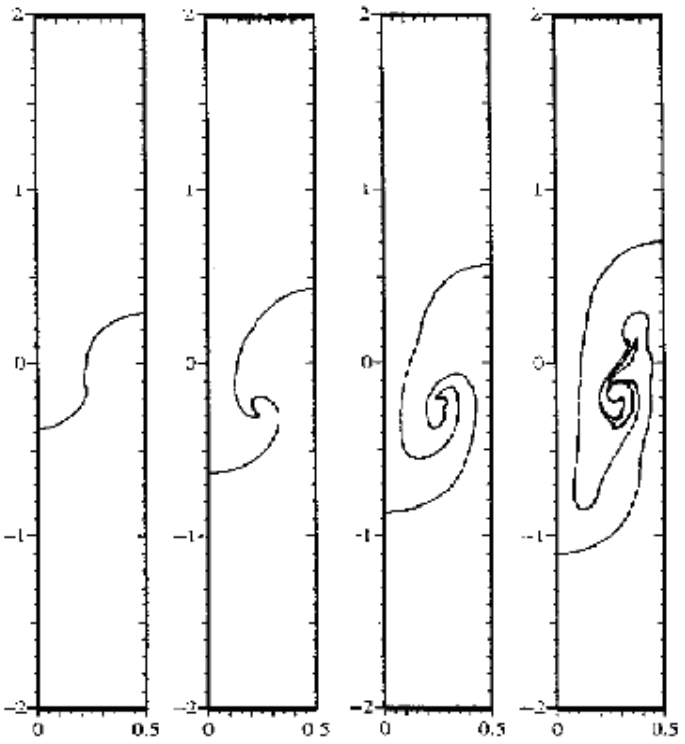

(b)

Figure3. Finger evolution (a) CE/SE and (b) Guermond 2000)

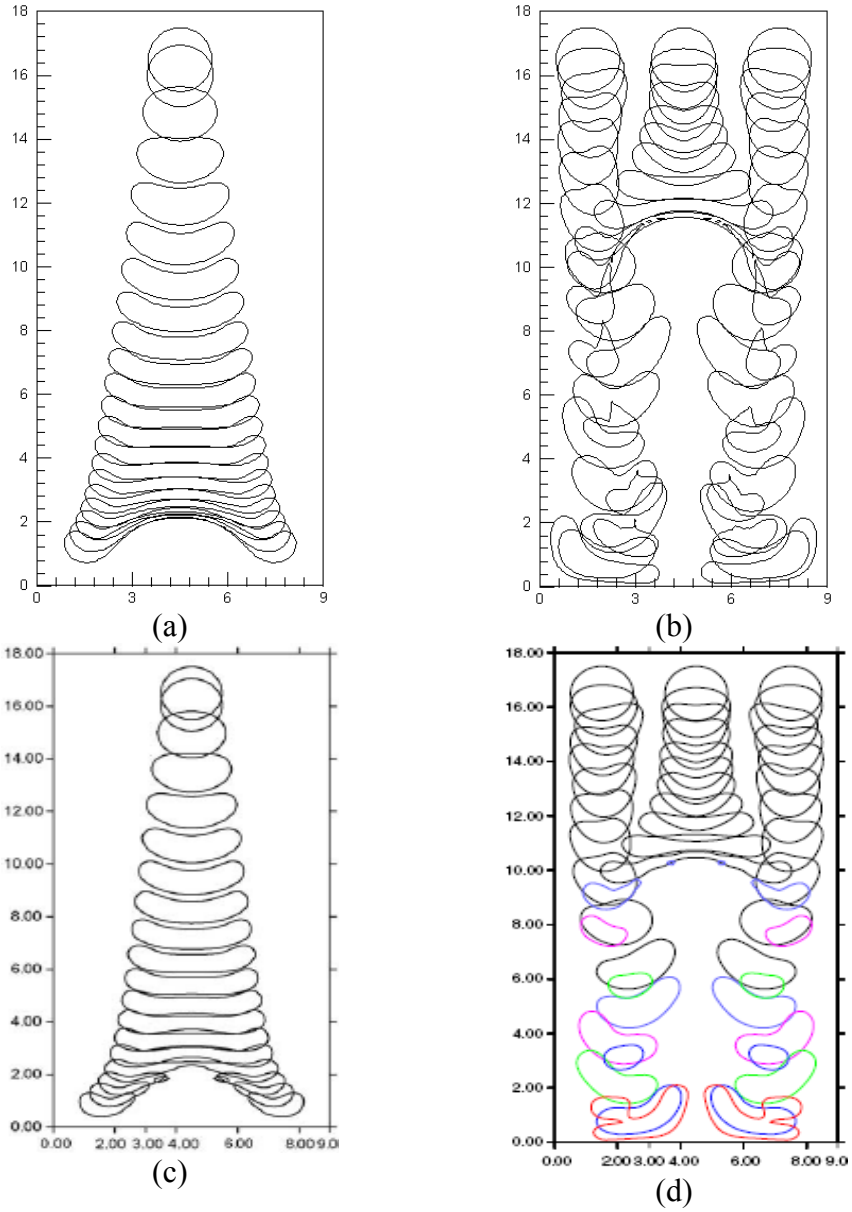

Figure 4. Deformation and motion of droplet (a) and (b) present CE/SE results and (c) and (d) denote FVM results [24].

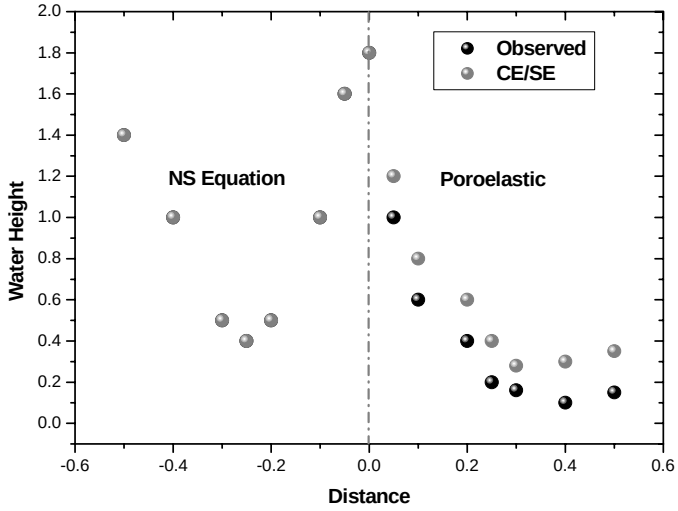

Figure 5. CE/SE calculated water height versus dimensionless distance in both clear and porous fluid

5. Dual Layer Lid-Driven Cavity Flows in Porous Medium

Lid-driven cavity flow has served as a benchmark for evaluating numerical schemes such are Ghia et al. [26] for orthogonal cavity and Dermirdzic et al. [27] for non-orthogonal cavity flows. Patil et al. [28] applied lattice Boltzmann method for simulating steady two-dimensional rectangular deep lid-driven cavity flow. Incompressible flow through isotropic granular porous media has been studied by Andrei et al. [29]. Al-Amiri [30] numerically investigated the effects of Darcy number and Richardson number on the flow and thermal behaviour for a lid-driven cavity filled with porous medium. Krishna et al. [31] numerically studied the effects of aspect ratio and skewness on flow behaviour for a lid-driven porous cavity. Yang et al. [15] numerically simulated the effects of Reynolds number, Darcy number (permeability) and porosity on the cavity flow field. The current studies involving lid-driven flows are primarily limited to either single-phase fluid or orthogonal square porous cavity. To the best of our knowledge, no work has been reported by considering dual layer lid-driven cavity flows in porous media based on the multiphase flow model.

Hence, it is critical to propose a benchmark problem for dual-layer lid-driven cavity flow in porous media. Here we set up a model for dual-layer lid-driven cavity flows in porous medium. The concept model of the dual layer lid-driven cavity flow is illustrated in figure6. The grid domain is 201×401. Avoiding the fluid instability, a light fluid is laid on the heavy fluid with different density and viscosity. The flow is driven by a lid with the velocity of 1.0 on the top boundary and all other boundaries are assigned to be on no-slip walls, as shown in figure6. We calculated eddies and vortex in the dual cavity for the porosity of 0.2 , We=20，Fr=1 and Reynolds number of 100. figure7-9 shows the stream lines and the interface for Darcy number of 10^2, 0.25 and 0.01, respectively. For individual Darcy number, the steady results show that the interface presents as a shear layer, which induced eddies and vortex. As the Darcy number increased sharply, the number of eddies and vortex were elevated, and the strength of eddies were enhanced, as expected. As the Darcy number varies from 0.25 to 10^2, the interface changes from horizontal lines to complex curly lines.

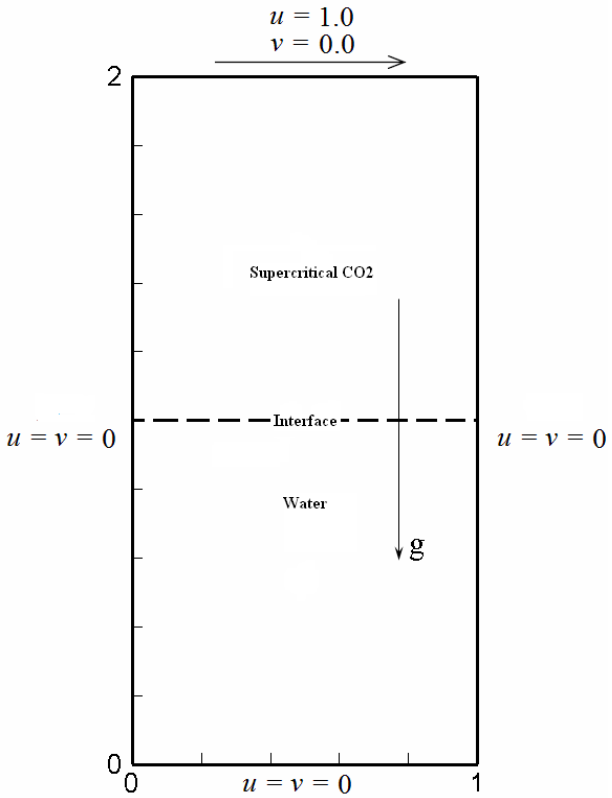

figure6. Schematic illustration of a dual layer lid-driven cavity flow

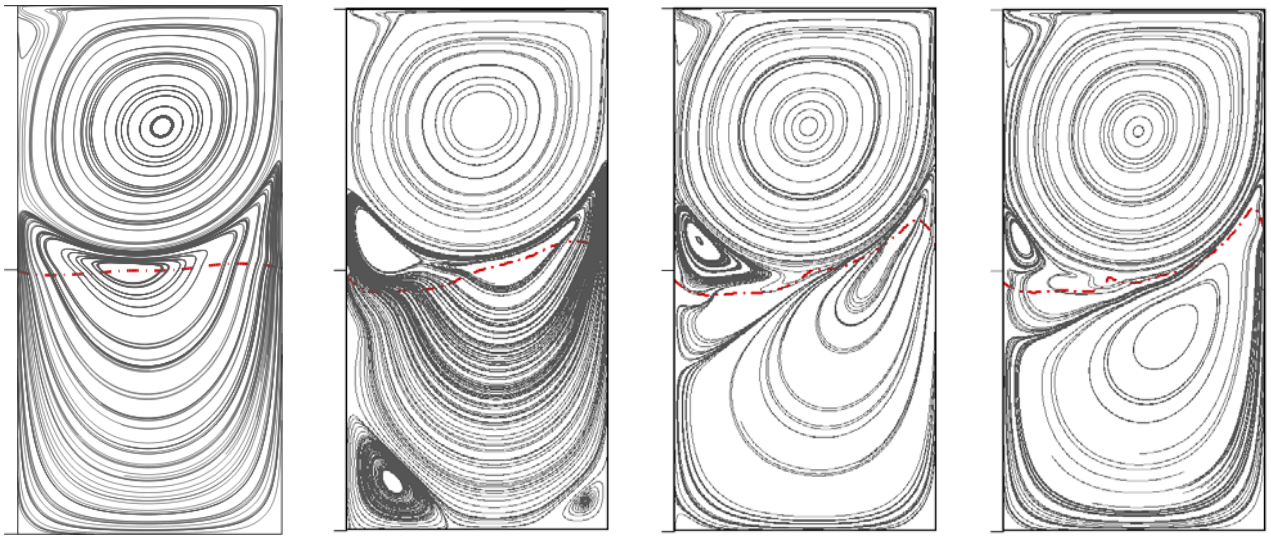

(a) (b) (c) (d)

figure7 Revolution of the interface and stream lines at time of (a) 50, (b) 100, (c) 150, (d) 200, respectively, for Darcy number 10^2 and viscosity ratio 50

Revolution of the stream lines and motion and deformation of the interface for *Da*=100 are shown in figure7. Dot lines present the stream lines, while dash lines denote the interfaces. At time of 50, formation of one secondary vortex takes place at the left upper corner caused by the shearing of the wall. The upper cavity is dominated by an eddy. In the down cavity there exists an eddy caused by the surface tension. The pattern of stream lines is analogue to the overlapping of two single cavity flows, which characterizes the basic property of the dual layer lid-cavity flow in porous media. The interface becomes slightly skewed, with the left side moving down and right side moving up. At time of 100, due to the surface tension effects, formation of two vortices take place in the bottom left and right, respectively, in the down cavity. The eddy strength becomes enhanced in the upper cavity, accompanied with one second vortex at the bottom left corner of the upper cavity, which results from the friction of the interface and the wall. The eddy in the down cavity moves up, towards the upper right. The interface deformation changes sharply and tends to move up, towards the upper right, as a curly line. At time of 150, two vortices at the left and right bottom vanish in the down cavity, while the eddy becomes stronger, and further moves up as a belt-shaped. Formation of the two vortices takes place at the left bottom and upper left corner in the upper cavity. The flow gradually tends to become stable. The interface nearly becomes parallel to the stream line. As time reaches to 200, the flow completely remains in the stable state, with the interface fully parallel to the stream line. The vortex becomes weaker at the bottom left in the upper cavity. Because of the shearing effects induced by the interface, there exists a vortex at the upper left corner in the down cavity. The eddy in the down cavity becomes enhanced. For Darcy number of 100, the energy generated by the moving lid is transferred into the down cavity.

Figure 8 illustrates the stream lines and the interface for different time at Darcy number of 0.25. Due to the increases of drag forces caused by the solid matrix, the energy generated by the moving lid was depleted by the motion of the interface. Hence, no secondary vortices take place, so that the reverse shear forces can't be induced. Therefore, the left side of the interface moves up, while the right side skews down. In the upper cavity, there only exists a skewed eddy at the upper right corner.

As shown in figure 9, the eddy slowly diminishes with further reduction of Darcy number to 0.01. That implied the drag forces are elevated remarkably. The energy generated by the moving lid can't be transferred into the deep cavity, due to the energy depletion resulting from the motion of the interface. There also no secondary vortices exists near the interface, hence, the interface almost

remains horizontal. Also, the viscous effect becomes more limited to the top region, as evidenced by the close spacing of the streamlines in figure 9. It can be observed that by the reduction of Darcy number from 100, eddies and vortices get reduced because of the obstruction for the flow due to the solid matrix. It's found that the lid-driven cavity flow in porous medium is significantly influenced by Darcy number for the Reynolds number and porosity considered. It notices that the flows mentioned above are in unstable state.

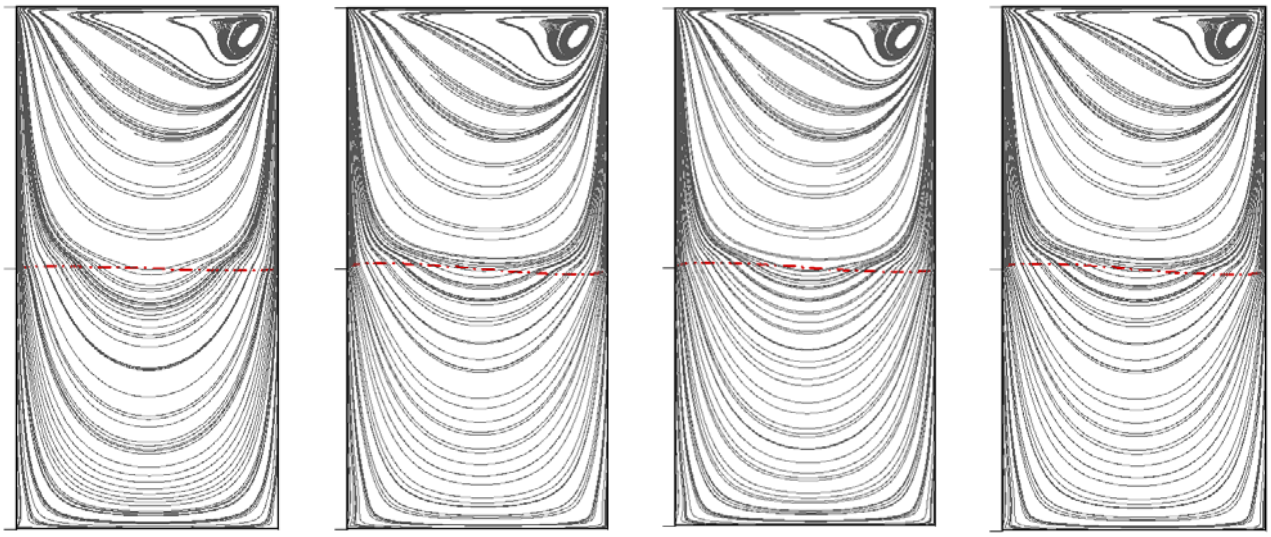

(a) (b) (c) (d)

Figure 8. Revolution of the interface and stream lines at time of (a) 50, (b) 100, (c) 150, (d) 200, respectively, for Darcy number 0.25 and viscosity ratio 50

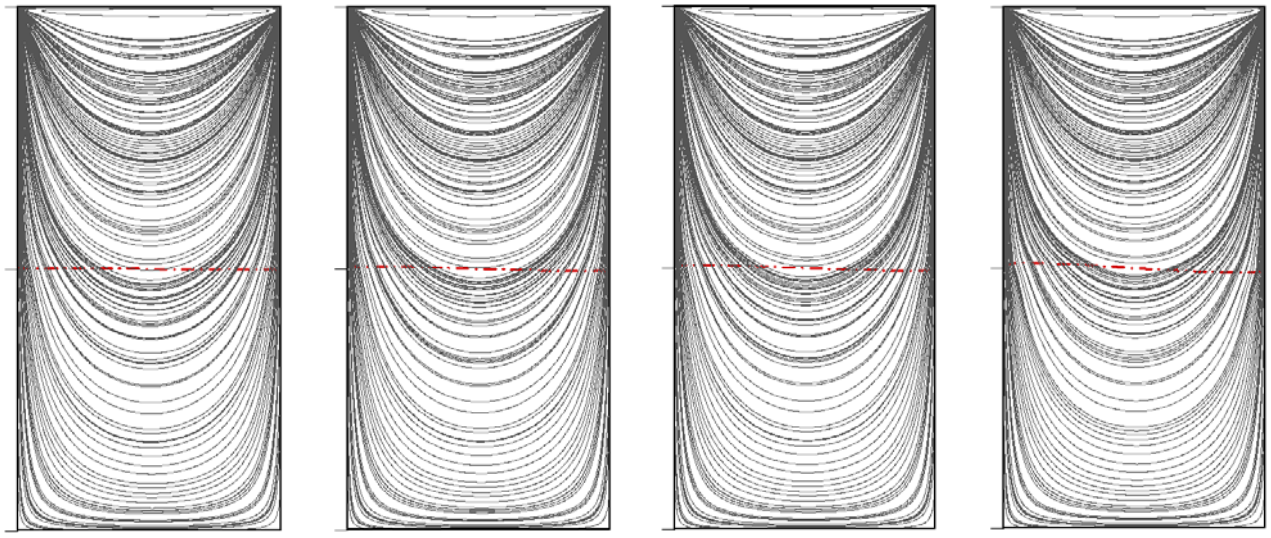

(a) (b) (c) (d)

Figure 9. Revolution of the interface and stream lines at time of (a) 50, (b) 100, (c) 150, (d) 200, respectively, for Darcy number 0.01 and viscosity ratio 50

From all results mentioned above the application of update high-order CE/SE method is successfully extended. It is an effective and reliable approach to calculate multiphase porous flow with interface, which can be treated accurately. CE/SE method has following advantages: it is easy to implement and programming, higher accuracy and efficiency.

6. Conclusion

In this paper, the second order accuracy CE/SE scheme, which is based on the hexahedron mesh, is proposed and used for simulations of multiphase flows in porous media. Further, the hybrid particle Level Set method is modified to accurately capture the fluid-fluid interface in porous flows. For validation and evaluation of the proposed method, Taylor instability problem, droplets falling problem and wave propagation in porous media are numerically simulated. Comparison between CE/SE calculated results and these of other literatures verified the reliability and accuracy of the updated CE/SE method. Furthermore, as a benchmark problem, the dual layer lid-driven porous cavity is developed and carefully simulated. Results show that the interface, as a shearing layer, has a great impact on the energy propagation into deep cavity, which is induced by the moving lid. We mainly study the effects of Darcy number on the revolution of stream lines and the motion and deformation of the interface. It indicates that Darcy number dominates the characteristics of the dual layer lid-driven porous cavity for the Reynolds number and porosity given. Future works will be completed by considering the effects of Reynolds number, porosity, aspect ratio and skewness on flow behaviour for this dual layer lid-driven porous cavity.

ACKNOWLEDGEMENT

The authors gratefully acknowledge the financial support of the National Natural Science Foundation of China (Grant No: 2008BAC38B04), and appreciate anonymous reviewers for significant comments. Duo-Xing Yang is a visiting researcher in Research Institute of Innovative Technology for the Earth (RITE).

NOMENCLATURE

$\vec{F}_{SV}$	continuum surface force
ϕ	level set function
δ	surface tension delta function
κ	interface front curvature
u_i	velocity component
φ	porosity
K	permeability
$H_\varepsilon(\phi)$	Heaviside function
P	pore pressure
$\bar{r}_p$	location of the particle
$\overline{V}$	particle velocity
E_3	Euclidean space
Re	Reynolds number
Fr	Froude number
We	Weber numbers
Da	Darcy number
x_i	space coordinate
t	time

References

[1] Guo, Z. and Zhao, T. A lattice Boltzmann model for convection heat transfer in porous media, Numer. Heat Transfer, 2005. Part B **47**, p.157–177.

[2] Yan, W., Liu, Y., Xu, Y. and Yang, X. Numerical simulation of air flow through a biofilter with heterogeneous porous media, Bioresource Technology, 2008. **99**, p. 2156–2161.

[3] Wang, J., Liu, K. and Zhang, D. An improved CE/SE scheme for multi-material elastic plastic flow and its applications, Comput Fluid, 2008. **38(3)**, p.544-551.

[4] Deiber, J. and Bortolozzi, R. A two-field model for natural convection in a porous annulus at high Rayleigh numbers, Chem Eng Sci, 1998. **53(8)**, p.1505-1516.

[5] Sman, R. Prediction of airflow through a vented box by the Darcy–Forchheimer equation, J Food Eng, 2002, **55**, p. 49–57.

[6] Costa, V., Oliveira, M. and Sousa, A. Numerical simulation of non-Darcian flows through spaces partially filled with a porous medium, Comput Struct, 2004. **82**, p.1535–1541.

[7] Reis, J., Griffiths, R. and Santos, J. Numerical simulation of the impact of liquid droplets on porous surfaces, J Comput Phys , 2004. **198**, p.747–770.

[8] Karim, M., Tanimoto, K. and Hieu, P. Modelling and simulation of wave transformation in porous structures using VOF based two-phase flow model, Applied Mathematical Modelling, 2009. **33**, p.343–360.

[9] Chang, S. A new approach for solving the Navier-Stokes and Euler equations,J Comput Phys, 1995. **119**, p.295–324.

[10] Chang, S., Wang, X. and Chow, C. The space-time conservation element and solution element method—a new high resolution and genuinely multidimensional paradigm for solving conservation law, J Comput Phys, 1999. **156**, p.89–136.

[11] Liu, K. and Wang, J. Analysis of high accuracy conservation-element and solution-element schemes, Chin Phys Lett, 2004. **21(11)**, p.2085–2088.

[12] Wang, X. and Chang, S. Prediction of sound waves propagating through a nozzle without/with a shock wave using the space-time CE/SE method, AIAA Paper ,2000. 2000-0222.

[13] Guo, Y., Wu, J., Yang, Z. and Oyediran, A.Extension of CE/SE method to 2D viscous flows, Comput Fluids, 2004. **33**, p.1349–1361.

[14] Yang, D., Zhang, D. and Li, G. A CE/SE scheme for flows in porous media and its applications, Aerosol Air Qual. Res, 2009. **9(2)**, p. 226-276.

[15] Yang,D. Zhang,D. and Zeng, R., et al. Calculation of multiphase flows in porous media based on CE/SE method, Chinese J. Geophys (in chinese), 2010. **53(1)**,p.189-196.

[16] Zhang, D., Wang, J. and Wang, G.. High order CE/SE method and applications, Chinse J. computational Physics (in chinese), 2009. **26(2)**, p.211-220.

[17] Osher, S. and Sethian, J. Fronts propagating with curvature dependent speed: algorithms based on Hamilton–Jacobi formulation, J Comput Phys, 1998. **79**,p.12-49.

[18] Enright, D., Fedkiw, R., Ferziger, J. and Mitchell, I. A hybrid particle level set for improved interface capturing, J Comput Phys,2002. **176**,p.205–227.

[19] Brackbill, J., Kothe,D. and Zemach, C., A continuum method for modeling of surface tension . J. Comput. Phys., 1992.**100**, p.335～354.

[20] Jiang,G. and Peng, D. Weighted ENO schemes for Hamilton--Jacobi equations,SIAM Journal on Scientific Computing, 2002. **21**, p.2126～2143.

[21] Yang, C. and Mao, Z. Numerical simulation of interphase mass transfer with the level set approach.Chem, Eng. Sci, 2005. **60**, p.2643-2660.

[22] Chorin, A. Numerical solution of the Navier Stokes equation, J. Comput. Phys., 1968. **22**, p.745-762.

[23] Guermond,G. and Quartapelle, L. A projection FEM for variable density incompressible flows, J. Comput. Phys., 2000. **165**,p.167-188.

[24] Ni, M, Komori, S and Morley, N. Direct simulation of falling droplet in a closet channel, Int. J. Heat Mass Transfer, 2006. **49**, p.366～376.

[25] Straughan,B. Effect of property variation and modelling on convection in a fluid overlying a porous layer, J. Comput. Phys.,2001.**170(1)**,p.320-337.

[26] Ghia, U., Ghia, K. and Shin, C., High-resolutions for incompressible flow using the Navier-Stokes equations and a multigrid method, J. Comput. Phys., 1982. **48**, p. 387-441.

[27] Dermirdzic, I., Lilek, Z. and Peric, M. Fluid flow and heat transfer test problems for non-orthogonal grids - Bench-mark solutions, International Journal for Numerical Methods in Fluids, 1992. **15**, p.329–354.

[28] Patil, D., Lakshmisha, K. and Rogg, B. Lattice Boltzmann simulation of lid-driven flow in deep cavities,Computers and Fluids, 2006. **35**,p.1116–1125.

[29] Andrei, B., Bourchtein,L.and Lukaszczyk,J. An arbitrary Lagrangian Eulerian computing method for all flow speeds, Applied Numerical Mathematics, 2002.**40**,p.291–306.

[30] Al-Amiri, A. Analysis of momentum and energy transfer in a lid-driven cavity filled with a porous medium,International Journal of Heat and Mass Transfer, 2000. **43**, p.3513–3527.

[31] Krishna,D., Basak,T. and Das, S. Numerical study of lid-driven cavity flow in orthogonal and skewed porous cavity, Commun. Numer. Meth. Engng , 2007. **24(10)**,p.815-831.